Hybrid Integral Equation and Finite Difference Method for Low-Frequency Electric Induction

Trevor W. Dawson, Sanjay Velamparambil * and Maria A. Stuchly
Department of Electrical and Computer Engineering University of Victoria,
P.O. Box 3055, Victoria, British Columbia, Canada, V8W 3P6

Abstract

Recently-developed fast integral equation solution methods allow for the treatment of electrostatic problems involving perfect conductors of complicated shape. Using the precepts of Stevenson's method, external electrostatic solutions can be used in the solution of internal low-frequency electric induction problems in electrically small isolated compact conducting bodies. A precorrected FFT algorithm is implemented to solve the electrostatic problem of an isolated human body situated in an external field. The resulting induced surface charge density serves as the source term for a finite-difference solution for the internal induced fields. It is shown that the resulting hybrid code produces results that are in excellent agreement with those produced by other methods, while being significantly more efficient in terms of computer memory and time resources.

1 Introduction

The theory of low-frequency electromagnetic induction in compact conducting bodies can be developed using Stevenson's method [1, §9.6]. The basic requirements are that the body be small compared to its own skin depth, which is in turn small compared to any relevant wavelength. The various internal and external phasor amplitudes can then be developed in wavenumber (or, equivalently, frequency) series. Maxwell's equations and the boundary conditions on the conductor provide a systematic scheme for solving for the various terms in the series, with fields of each order forming part of the excitation for those of next higher order.

This approach provides a particularly useful framework for solving low-frequency induction problems such as those involving bioelectromagnetic effects associated with power-line frequency (50-60 Hz) fields. Here the zeroth- and first-order fields are of most interest. The essential results are that (i) the lowest-order incident magnetic field is static and is unperturbed by the conductor, (ii) the lowest-order external electric field is static, with the body serving as a perfect conductor, and (iii) the internal electric field is first-order in frequency, and has the static magnetic field and surface charge density as its sources [1].

The two source terms can be considered independently by linear superposition. The focus of the present work is induction by electric fields. The most significant complication in this situation is the perturbation of the incident external field by the conductor. Although this must be accounted for in any modelling, the solution is hampered by the unbounded exterior domain, most particularly with any finite-difference based method.

Finite element methods would offer an alternative solution method, but suitable high-resolution models are not readily available. The conductivity models used in bioelectromagnetic modeling are typically voxel-based and lend themselves readily to finite-difference solution methods. Two such methods that have successfully been applied solve for the internal and external fields simultaneously. The first is a finite-difference method with the external domain being handled with an expanding mesh [2]. The second is a recently-developed quasistatic finite-difference time-domain (QSFDTD) method [3]. Here the external problem is handled by a very short time simulation and absorbing boundary conditions located close to the conductor. The QSFDTD method works well in practice, and can handle both plane wave and line sources (of both electric and magnetic type) [4]. It is however, a vector method, and computer memory and time constraints rapidly become prohibitive.

*Center for Computational Electromagnetics, Electrical and Computer Eng, Univ. of Illinois at Urbana-Champaign

Alternative approaches based on Stevenson's method handle the problem in two stages. The internal problem can be solved independently, if the static surface charge density is available. One recently-published method for handling higher-resolution problems used a hybridization of the QSFDTD with an efficient frequency-domain scalar-potential finite-difference (SPFD) code [5]. In this approach, the QSFDTD is applied to a lower-resolution model, and the associated surface charge density distribution obtained. This is then extrapolated onto the surface of a higher-resolution model, to serve as the boundary conditions for a run of the SPFD code. The hybrid scheme was shown to be practical and efficient for estimating the higher resolution induced fields fixed computer resources. A weak point in the approach is the extrapolation process, as it involves the surfaces of two comparable but distinct voxel-based models.

Within the limitations of voxel-based models, however, it would be preferable to obtain the correct surface charge distribution for a given model for direct input to the SPFD code. The solution to the external electrostatic problem can be formulated in terms of an integral equation over the conductor surface [1, Ch.4]. In principle, the integral equation provides a domain reduction and the associated free-space electrostatic Green's function kernel handles the unbounded domain. This raises of the idea of solving the integral equation using the surface facets of the model in question. However, any direct solution scheme involves a dense coefficient matrix and again rapidly becomes prohibitive. For example, the results in this paper are based on two human body models, having resolutions of 7.2 and 3.6 mm, respectively. The former has 49438 surface facets, while the latter has 200062. The coefficient matrix associated with a solution of the latter problem would contain over 4×10^{10} entries, and a direct solution is clearly out of the question.

However, recently developed fast methods make solution of the integral equation practical. The first point is that the $1/R$ Green's function has a simple closed form. The second point is that iterative linear system solvers only require matrix-vector products, and need no direct access to the underlying coefficient matrix. A third point is that the integral equation is in convolution form, and a solution by Fast Fourier transforms would be possible, aside from the restriction to the body surface. These features are at the heart of the pre-corrected fast Fourier transform (PCFFT) method [6]. The continuous surface charges are replaced with an equivalent volume distribution of discrete point charges on a regular Cartesian grid containing the conductor. These discrete charges can be chosen in such a way that their potential approximates, to any desired accuracy, the potential due to the actual sources at sufficiently large distances. Thus, interactions between facets that are sufficiently separated can be computed efficiently using the volume grid charges and FFTs. Interactions between nearby facets are computed directly. Once the solution is available, the volume charges can be mapped back to the facets of the original model to obtain the required surface charge density distribution. This is then converted to equivalent point charges at the surface nodes of the body model. The resulting data is in perfect alignment for use in the boundary conditions for a subsequent SPFD solution of the internal problem.

In this work, it is shown that an implementation of the PCFFT method provides an efficient and practical method for computing the surface charges on the voxel-based human body models. It is shown that excellent agreement is obtained between results from the QSFDTD, QSFDTD+SPFD hybrid, and PCFFT+SPFD hybrid methods, for both vertical uniform field and a horizontal overhead line charge.

2 Methods

In this section, the body models are described briefly. Next, the equations governing the dominant internal and external electric fields using Stevenson's method are indicated. Finally a summary of the various numerical methods is given.

2.1 Body Models

The human body models used in this work are anatomically derived. They comprise cubic voxels, each of which is assigned electrical properties appropriate to its associated tissue at 60 Hz. Two model resolutions are used. The low-resolution model comprises 204547 voxels with 7.2-mm edges, while the high-resolution model has 1639143 voxels 3.6-mm edges. Figure 1 shows an external view of the high resolution model. The models are more fully described elsewhere [7].

2.2 External Problem

The time-harmonic electric field has the form

$$\boldsymbol{e}(\boldsymbol{x},t) = \Re\left\{\boldsymbol{E}(\boldsymbol{x})\, e^{+j\omega t}\right\}. \qquad (1)$$

In the absence of any applied magnetic field, the dominant electric field amplitude outside the body is static

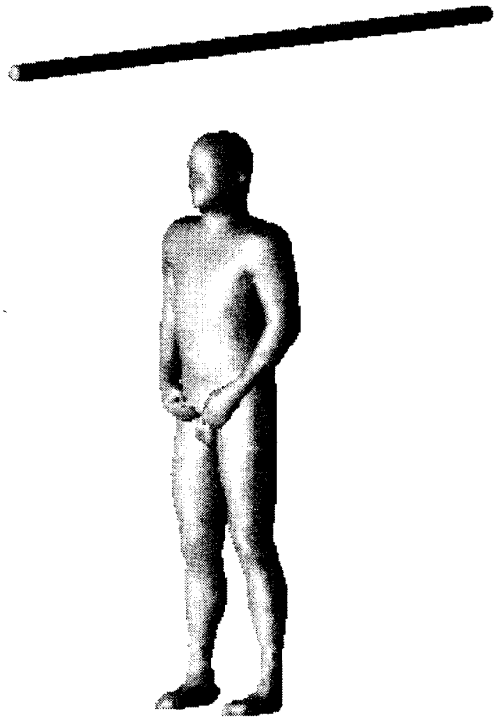

Figure 1: Surface view of the body model and a segment of the line source.

and has the representation

$$\boldsymbol{E}^e(\boldsymbol{x}) = -\nabla\varphi(\boldsymbol{x}). \tag{2}$$

The potential satisfies

$$\nabla^2\varphi(\boldsymbol{x}) = -\rho^s(\boldsymbol{x})/\varepsilon_0, \tag{3}$$

where $\rho^s(\boldsymbol{x})$ is the static limit of the volume charge density associated with the external sources. The potential can be decomposed as

$$\varphi(\boldsymbol{x}) = \varphi^b(\boldsymbol{x}) + \varphi^s(\boldsymbol{x}), \tag{4}$$

where φ^s is the potential due to the sources in the absence of the body and φ^b is the potential due to the induced surface charge on the body. The former satisfies (3) subject to appropriate boundary conditions at infinity. The latter satisfies (3) with zero right-hand side. The boundary condition is that the body surface be an equipotential,

$$\varphi^b(\boldsymbol{x}) + \varphi^s(\boldsymbol{x}) = \varphi_0. \tag{5}$$

This potential is unknown, and must be determined from the constraint that the body have zero net charge. The problem can be converted to the integral equation form [1]

$$\varphi^s(\boldsymbol{x}') + \frac{1}{4\pi\varepsilon_0}\oiint_{\mathcal{B}} \frac{\eta(\boldsymbol{x})}{\|\boldsymbol{x}-\boldsymbol{x}'\|}\,da(\boldsymbol{x}) = \varphi_0, \quad (\boldsymbol{x}' \in \mathcal{B}), \tag{6}$$

where $\mathcal{B}$ denotes the body surface and $\eta(\boldsymbol{x})$ is the associated static surface charge density. The integral equation is to be solved subject to the constraint

$$\oiint_{\mathcal{B}} \eta(\boldsymbol{x})\,da(\boldsymbol{x}) = 0, \tag{7}$$

the left-hand side being the total induced charge.

2.3 Internal Problem

The body has the conductivity distribution $\sigma(\boldsymbol{x})$. The electric field inside the body has the representation

$$\boldsymbol{E}^i(\boldsymbol{x}) = -\nabla\psi(\boldsymbol{x}), \tag{8}$$

and is governed by the condition that the current density, $\boldsymbol{J}(\boldsymbol{x}) = \sigma(\boldsymbol{x})\boldsymbol{E}(\boldsymbol{x})$, have zero divergence

$$\nabla\cdot\boldsymbol{J}(\boldsymbol{x}) = 0, \quad (\boldsymbol{x} \in \mathcal{V}), \tag{9}$$

in the body interior $\mathcal{V}$. Consequently, the internal potential satisfies

$$\nabla\cdot[\sigma(\boldsymbol{x})\nabla\psi(\boldsymbol{x})] = 0, \quad (\boldsymbol{x} \in \mathcal{V}). \tag{10}$$

The internal fields are governed by the boundary condition

$$\hat{\boldsymbol{n}}(\boldsymbol{x})\cdot\boldsymbol{J}(\boldsymbol{x}) = -j\omega\eta(\boldsymbol{x}), \quad (\boldsymbol{x} \in \mathcal{B}), \tag{11}$$

expressing charge conservation. Here $\eta(\boldsymbol{x})$ is the static surface charge obtained from solution of the external problem, and $\hat{\boldsymbol{n}}(\boldsymbol{x})$ is the local outward normal unit vector. This translates to the boundary condition

$$\sigma(\boldsymbol{x})\hat{\boldsymbol{n}}(\boldsymbol{x})\cdot\nabla\psi(\boldsymbol{x}) = j\omega\eta(\boldsymbol{x}), \quad (\boldsymbol{x} \in \mathcal{B}), \tag{12}$$

on the internal potential. Finite difference approximation of equations (10) and (12) forms the basis of the SPFD method for low-frequency electric induction.

One additional point worth noting concerns conductors containing internal air cavities. The fields in such cavities are not computed directly by the SPFD method, since they do not directly affect the fields in the conductor. These fields can, however, be computed once the conducting potential is found. They can be derived from a harmonic potential, driven by boundary conditions of continuity of tangential electric field at the conductor boundary. Thus the field within the j^{th} cavity, $\mathcal{C}_j$, can be expressed as

$$\boldsymbol{E}(\boldsymbol{x}) = -\nabla\psi_j^0(\boldsymbol{x}), \quad (\boldsymbol{x} \in \mathcal{C}_j). \tag{13}$$

Each cavity potential satisfies Laplace's equation

$$\nabla^2 \psi_j^0 (\boldsymbol{x}) = 0, \quad (\boldsymbol{x} \in \mathcal{C}_j), \tag{14}$$

within its associated volume, subject to continuity of the cavity and conductor potentials

$$\psi_j^0 (\boldsymbol{x}) = \psi (\boldsymbol{x}), \quad (\boldsymbol{x} \in \partial\mathcal{C}_j), \tag{15}$$

on the cavity walls.

2.4 Numerical Methods

Three numerical methods are used in computing the results in this paper. The first is the QSFDTD method [3]. This is based on a full solution of Maxwell's equations. The second is the hybrid two-stage QSFDTD+SPFD method where the QSFDTD solution is used to compute the static surface charge, and the SPFD method used to compute the internal fields [5]. The third method is a newly-implemented hybrid PCFFT+SPFD method. The PCFFT method [6] is used to solve (6) and (7) to compute the static surface charge, and the SPFD method again used subsequently to solve the interior problem.

3 Results

Two source configurations are considered. The first is a 60-Hz, 1-kV/m (peak) electric field parallel to the long axis of the body. The second is an infinite line charge source producing a 60-Hz electric field normalized to 1-kV/m (peak) level at a radial distance of 1 m from the wire centre. The line passes 0.26 m above the top of the head, and is centered from left-to-right, with the model looking along the wire as indicated in Figure 1.

Both configurations are run using the three numerical methods. The full QSFDTD results are used as a benchmark. The hybrid QSFDTD+SPFD results at each fixed resolution are included to further validate the implementation of Stevenson's method for the interior solution. In addition, the hybrid QSFDTD+SPFD is run using the low-resolution surface charge density extrapolated onto the 3.6-mm model, for a total of 7 data sets. This last set is to demonstrate that the hybrid PCFFT+SPFD method gives results in closer agreement to the high-resolution QSFDTD data than the QSFDTD+SPFD method involving charge extrapolation.

To demonstrate the overall agreement between the various computations using the high-resolution model, Table I presents several measures of the assorted whole-body temporal rms electric fields, as well as comparisons among them. The upper part of the table pertains to the whole-body data sets, and gives the volumetric maximum, average and rms values taken solely over voxels belonging to the body model. Column A pertains to data obtained from the QSFDTD code, considered as the reference solution. Column B contains data computed by the hybrid QSFDTD+SPFD method at the same resolution. Results from the hybrid PCFFT+SPFD method are in Column C. The final column is obtained by extrapolating the surface charge density taken from a low-resolution (7.2 mm) QSFDTD run onto the high-resolution (3.6 mm) model for an SPFD interior computation.

The central part of the table details the resulting discrepancies among the various numerical schemes. Each data set from columns B through D is subtracted voxel-by-voxel from the QSFDTD reference solution to create a set of whole-body difference fields. The indicated measures pertain to these various difference fields. The rows for the minimum, maximum and average respect the signs of the differences in the computation, while the row labelled "Avg.Abs" is for the absolute value of the difference fields.

The lower line of the table is a measure of the whole-body correlation coefficient between each calculation and the reference solution.

The next set of results present a closer look at the discrepancies. Figure 2 shows the total vertical current as a function of height above the soles of the feet, for the uniform external field on the left and the line source on the right. Each panel contains three curves. Two are from the QSFDTD computations based on each model resolution. The third is from the QSFDTD+SPFD hybrid method involving the charge density extrapolation process.

A detailed indication of the differences is presented in Figure 3. The central panel shows the total vertical induced current as a function of height above the soles of the feet for the two sources, based on the high-resolution QSFDTD calculations. The two flanking panels indicate on a logarithmic scale errors of the the three alternative high-resolution calculations relative to the QSFDTD results as a function of height. The left panel pertains to the uniform source and the right panel to the line source.

Table II presents various volumetric measures of the temporal rms electric fields induced in the skin by the two sources as computed by the various numerical methods in both model resolutions. The first col-

	A QSFDTD3.6	B QSFDTD3.6 +SPFD3.6	C PCFFT3.6 +SPFD3.6	D QSFDTD7.2 +SPFD3.6
Max.	6.5293	6.5290	6.4792	6.5902
Avg.	0.3245	0.3245	0.3224	0.3290
RMS	0.5500	0.5400	0.5366	0.5400
		A-B	A-C	A-D
Min.		-1.937×10^{-3}	-5.558×10^{-2}	-2.460×10^{-1}
Max.		$+1.268 \times 10^{-3}$	$+2.445 \times 10^{-1}$	$+3.078 \times 10^{-1}$
Avg.		-6.237×10^{-6}	$+2.092 \times 10^{-3}$	-4.444×10^{-3}
Avg.Abs.		$+6.313 \times 10^{-5}$	$+2.164 \times 10^{-3}$	$+6.898 \times 10^{-3}$
RMS		$+1.213 \times 10^{-4}$	$+4.304 \times 10^{-3}$	$+1.221 \times 10^{-2}$
Std.Dev.		$+9.499 \times 10^{-8}$	$+3.989 \times 10^{-6}$	$+1.057 \times 10^{-5}$
1-Corr.		$+1.532 \times 10^{-8}$	$+7.397 \times 10^{-6}$	$+1.348 \times 10^{-4}$

Table I: Measures of, and comparisons between, the whole-body temporal rms electric field modulus for various high-resolution computations under line source excitation.

Source	Method	Model	Std.Dev.	Average	RMS	Maximum	L95	L99
Line	QSFDTD	3.6	0.4806	0.4926	0.6882	5.2524	1.3937	2.6014
Line	QSFDTD+SPFD	3.6	0.4800	0.4924	0.6876	5.2439	1.3916	2.5972
Line	PCFFT+SPFD	3.6	0.4716	0.4792	0.6723	5.1780	1.3730	2.5640
Line	QSFDTD+SPFD	7.2 + 3.6	0.4728	0.4965	0.6855	5.2142	1.4361	2.5300
Line	QSFDTD	7.2	0.4306	0.4918	0.6536	3.9930	1.3449	2.3002
Line	QSFDTD+SPFD	7.2	0.4303	0.4914	0.6532	3.9867	1.3428	2.2967
Line	PCFFT+SPFD	7.2	0.4179	0.4765	0.6338	3.9320	1.3230	2.2650
Uniform	QSFDTD	3.6	0.6136	0.5407	0.8179	6.9150	1.7650	3.3550
Uniform	QSFDTD+SPFD	3.6	0.6129	0.5404	0.8172	6.9050	1.7620	3.3500
Uniform	PCFFT+SPFD	3.6	0.6057	0.5271	0.8029	6.8260	1.7420	3.3120
Uniform	QSFDTD+SPFD	7.2 + 3.6	0.5938	0.5367	0.8004	6.8240	1.6730	3.2420
Uniform	QSFDTD	7.2	0.5616	0.5260	0.7694	5.5610	1.6980	3.0320
Uniform	QSFDTD+SPFD	7.2	0.5612	0.5256	0.7689	5.5540	1.6960	3.0280
Uniform	PCFFT+SPFD	7.2	0.5481	0.5103	0.7489	5.4750	1.6170	2.9300

Table II: Various measures of the temporal RMS electric fields (mV/m) induced in the skin.

Source	Method	Model	Std.Dev.	Average	RMS	Maximum	L95	L99
Line	QSFDTD	3.6	0.2290	0.5793	0.6230	2.4098	0.9560	1.2869
Line	QSFDTD+SPFD	3.6	0.2289	0.5789	0.6225	2.4084	0.9553	1.2862
Line	PCFFT+SPFD	3.6	0.2264	0.5717	0.6149	2.3760	0.9424	1.2690
Line	QSFDTD+SPFD	7.2 + 3.6	0.2475	0.6220	0.6695	2.6319	1.0225	1.3831
Line	QSFDTD	7.2	0.1947	0.6694	0.6971	1.8300	0.9998	1.1915
Line	QSFDTD+SPFD	7.2	0.1946	0.6691	0.6968	1.8293	0.9991	1.1915
Line	PCFFT+SPFD	7.2	0.1897	0.6517	0.6787	1.7800	0.9722	1.1590
Uniform	QSFDTD	3.6	0.1427	0.3450	0.3733	1.4670	0.5820	0.7691
Uniform	QSFDTD+SPFD	3.6	0.1426	0.3447	0.3730	1.4660	0.5816	0.7685
Uniform	PCFFT+SPFD	3.6	0.1409	0.3402	0.3682	1.4490	0.5745	0.7593
Uniform	QSFDTD+SPFD	7.2 + 3.6	0.1530	0.3683	0.3988	1.5640	0.6199	0.8194
Uniform	QSFDTD	7.2	0.1193	0.3949	0.4125	1.1280	0.5895	0.7091
Uniform	QSFDTD+SPFD	7.2	0.1193	0.3947	0.4123	1.1270	0.5892	0.7088
Uniform	PCFFT+SPFD	7.2	0.1164	0.3847	0.4020	1.1000	0.5752	0.6919

Table III: Various measures of the temporal RMS electric fields (mV/m) induced in the brain.

Source	Method	Model	Std.Dev.	Average	RMS	Maximum	L95	L99
Line	QSFDTD	3.6	0.1505	0.4921	0.5146	1.2014	0.7863	0.9440
Line	QSFDTD+SPFD	3.6	0.1504	0.4920	0.5145	1.2007	0.7863	0.9433
Line	PCFFT+SPFD	3.6	0.1496	0.4890	0.5113	1.1940	0.7820	0.9385
Line	QSFDTD+SPFD	7.2 + 3.6	0.1563	0.5134	0.5366	1.2480	0.8174	0.9808
Line	QSFDTD	7.2	0.1200	0.4356	0.4518	0.8662	0.6620	0.7517
Line	QSFDTD+SPFD	7.2	0.1199	0.4352	0.4514	0.8655	0.6615	0.7509
Line	PCFFT+SPFD	7.2	0.1183	0.4290	0.4450	0.8535	0.6527	0.7412
Uniform	QSFDTD	3.6	0.1432	0.4527	0.4748	1.1370	0.7252	0.8840
Uniform	QSFDTD+SPFD	3.6	0.1431	0.4526	0.4747	1.1370	0.7249	0.8837
Uniform	PCFFT+SPFD	3.6	0.1423	0.4495	0.4715	1.1300	0.7204	0.8782
Uniform	QSFDTD+SPFD	7.2 + 3.6	0.1470	0.4672	0.4898	1.1700	0.7459	0.9092
Uniform	QSFDTD	7.2	0.1106	0.3844	0.4000	0.7770	0.5885	0.6812
Uniform	QSFDTD+SPFD	7.2	0.1105	0.3841	0.3996	0.7763	0.5879	0.6806
Uniform	PCFFT+SPFD	7.2	0.1090	0.3785	0.3939	0.7654	0.5796	0.6710

Table IV: Various measures of the temporal RMS electric fields (mV/m) induced in the heart.

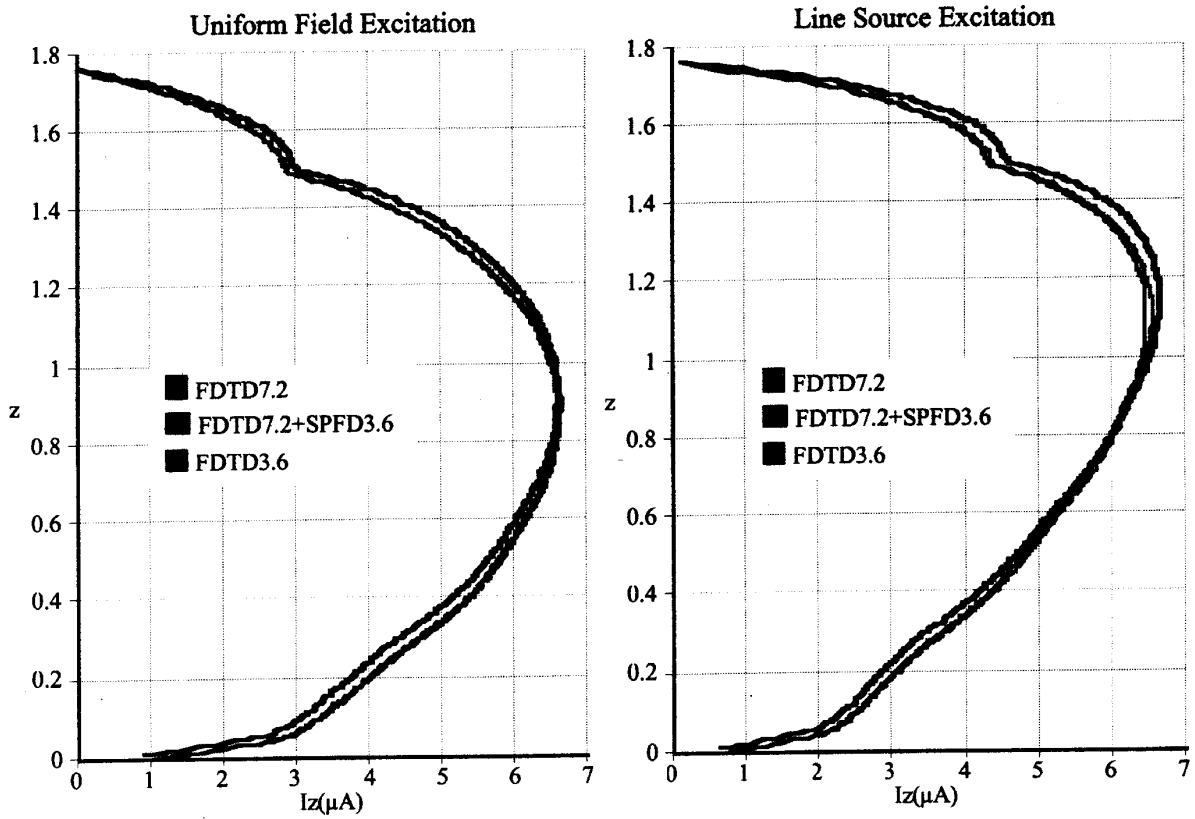

Figure 2: Comparison of total vertical current as a function of height above the soles of the feet for the line current and uniform electric field sources for the two model resolutions (lighter curves) obtained by the quasistatic FDTD code, together with the data from the high-resolution data obtained using SPFD with charge extrapolation from the low-resolution FDTD data.

umn indicates the source. The second column indicates the numerical method (either the quasistatic FDTD reference method or one of the two hybrid methods). The third column indicates the model resolution used in millimeters. The rows labelled "7.2 + 3.6" indicate use of the charge density extrapolation algorithm. The various volumetric measures included are the standard deviation (as a measure of the variation of the field across the tissue), the average, the root-mean-square, and maximum. The final two columns, labelled "L95" and "L99" are the field values not exceeded in 95% and 99%, respectively, of the voxels comprising the tissue. All tabulated values are in mV/m.

Finally, Table III is analogous to Table II, but for the brain. Table IV presents the corresponding results for the heart.

4 Discussion

The goal of the research underlying this work is to compute induced bioelectromagnetic fields as accurately as possible. This requires efficient computational methods for moving to higher resolution and the associated increased realism of the models. At the same time, it is essential that the numerical schemes be well-validated.

The QSFDTD code has proved to be a useful tool, but is increasingly demanding of computer resources as the resolution increase. Each doubling of resolution increases the memory requirements by a factor of 8 and the computational time by a factor of 16. The whole-body high-resolution QSFDTD computations have only recently become feasible at our laboratory. One additional point is worth mentioning. The quasistatic FDTD code used for this work is entirely distinct from that used for earlier work [3], providing an additional check on the coding.

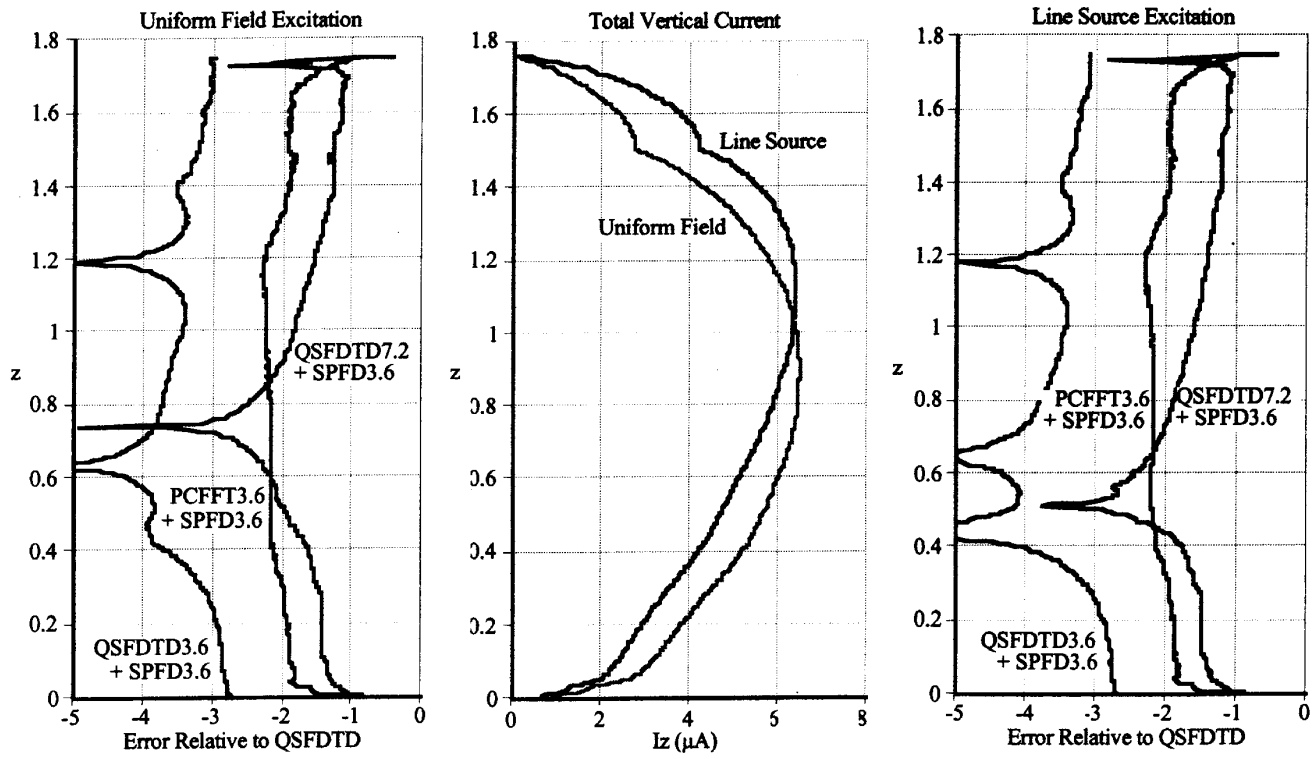

Figure 3: Total vertical current as a function of height above the soles of the feet for the line current and uniform electric field sources (center panel), with $\log_{10}$ relative errors of three high-resolution computations compared to the quasistatic FDTD results for the uniform field (left) panel and line source (right panel) sources.

The hybrid QSFDTD+SPFD calculations at a fixed resolution are redundant, since the internal electric fields can be extracted from the QSFDTD data. They are included to validate the precepts and implementation of Stevenson's method. The bottom row of Table I indicates the almost-perfect agreement between the two calculations at a fixed resolution. A correlation coefficient of 1 would indicate a perfect match (apart from a scale factor) and would lead to a value of 0 in the table. One point worth noting is that the recent addition of the cavity field computation brings the hybrid QSFDTD+SPFD results into almost perfect agreement with the straight QSFDTD data. Such was not the case in earlier work [8], where the cavity fields were not computed in the SPFD portion of the calculation. These results provide validation of the *postpriori* computation of the SPFD cavity fields.

The principal reason for the development of the hybrid QSFDTD+SPFD code [5] was to allow for charge extrapolation and use of more efficient SPFD code for the internal calculations at higher resolution. The fifth column indicates the resulting algorithm provides reasonable agreement, and remains a viable scheme.

The fourth column of the table indicates that the hybrid PCFFT+SPFD in fact provides closer agreement with the reference solution than that obtained from the QSFDTD+SPFD hybrid code with extrapolation. This is confirmed by the other results. The increased agreement is due to the ability of the PCFFT solution to more accurately account for differences in detail between the two model resolutions.

In Figure 2, the QSFDTD vertical current curves obtained from the two models are virtually indistinguishable from each other on the plots. This result may be expected, since the models are closely related and the vertical current depends largely on body shape. Computation of the high-resolution QSFDTD data was not possible with the computer resources available at the time the interpolation algorithm was published [5]. The present work illustrates the slight deficiencies in the latter process. The hybrid data are represented by the darker lines. They are in reasonable agreement with the direct QSFDTD results, but overestimate the

vertical current in the upper part of the body and underestimate it in the lower part.

The deficiencies of the extrapolation algorithm and superior performance of the integral equation based hybrid algorithm are further indicated in Figure 3. The central panel containing the high-resolution reference curves shows the expected result that the the non-uniform line source field is associated with higher currents closer to the head [4]. Since the vertical current curves produced by the various computational methods are virtually indistinguishable in a common plot, the flanking panels show the relative differences on a logarithmic scale. These clearly indicate the superior performance of the (accurate but redundant) QSFDTD+SPFD hybrid calculation at the fixed resolution, with the error being generally less than 0.1%. These results do, however, provide a useful validation of the correctness of the two distinct computer codes. It is also apparent that the QSFDTD+SPFD hybrid calculation with extrapolation is the least accurate relative to the reference solution, with errors of the order of 3%-10%. The final point illustrated by the first and third panels is that the new PCFFT+SPFD hybrid data are in generally excellent agreement, with the errors relative to the QSFDTD reference data being of the order of 1%.

Since the principal applications of the codes described here are presently to bioelectromagnetic problems, it is of interest to examine the results produced by the various codes at a finer level. This is of particular importance if numerical modeling is to play a role in the setting of protection standards for human exposure to low frequency electric and magnetic fields. This purpose is addressed in Tables II through IV.

The skin data are not particularly realistic due to the sharp corners and associated field singularities inherent in the voxel-based computations [9]. However, this information is useful in illustrating the nature of the discrete surface charge representations.

Both finite difference codes assign the primary electric field mesh to the edges of the material voxels. The voxel vertices form a set of nodes. The conducting model may then be viewed as a lattice of discrete resistors associated with each edge and connecting the nodes. An edge contacting at least one body voxel is termed "internal", while an edge surrounded by four external air voxels is termed "external". In the post-processing of the QSFDTD data to obtain the physical quasistatic fields, internal edge fields are typically a factor of 10^6 (mV/m) smaller than external edge fields (kV/m) in the present situation. The QSFDTD code thus only gives rise to static surface charges at "exterior" boundary nodes, defined as having at least one external edge. For example, the high-resolution model has a total of 200051 surface nodes, of which 131502 are exterior. The low resolution model has 33145 exterior nodes out of a total of 49368 surface nodes. The hybrid QSFDTD+SPFD hybrid code only makes use of the exterior node charges.

In contrast, the integral equation based approach works with the surface facets of the model. The implementation used in the present calculations assumes a constant surface charge density on each boundary facet. After solution for the facet charge densities, charges are assigned at every boundary node by attributing one quarter of each facet's total charge to each of its four corner nodes.

The result is that a different discrete surface charge representation is used in each of the two hybrid codes. The overall consequences are clearly not very significant. For example, Table II shows that the standard deviations computed by the QSFDTD and hybrid QSFDTD+SPFD differ in the fourth decimal place, while the hybrid PCFFT+SPFD data differ in the second, in either model resolution. Similarly, the hybrid PCFFT+SPFD data are associated with slightly less-singular surface fields, evident in the maximum, L95 and L99 values. Thus despite the different surface charge descriptions, the electric field measures computed from the hybrid PCFFT+SPFD code generally agree with the reference solution values to at least two significant figures.

The remaining two tabulated comparisons are of more interest in a bioelectromagnetic context. These pertain to the heart and brain, both of which contain excitable tissue and are relevant in the setting of protection standards. Since these organs are internal to the body, less discrepancy in the numerical results might be expected. In fact, Table III shows that the hybrid PCFFT+SPFD data generally agree with the reference solution to three significant figures, for both source types and for both model resolutions. A similar comment applies to the heart data in Table IV.

Comments on the relative efficiency of the methods are in order, based on computer resources presently available to us. A full QSFDTD solution based on the high-resolution model uses 9800 time steps of 6.86 ps and requires 1.9 GB of memory and over 18 hours using 6 processors on an IBM SP2 SMP machine. A solution for the low-resolution model can be obtained in roughly 2 hours on the same machine, and in approximately 16 hours on a 4-processor SGI Origin 2000 machine (with an approximate 16-fold time increase for the high resolution model). In contrast, once the surface charge data

is available, the SPFD code requires roughly 1 hour on the SGI machine for a high-resolution run and of the order of 15 minutes for a low-resolution computation. The PCFFT code requires about 2 hours to compute the surface charge distribution on the high-resolution model, and less than 0.5 hours for the low-resolution one, using a single processor on the SGI machine. A complete hybrid PCFFT+SPFD solution for the 3.6-mm model thus takes approximately 3 hours on the SGI box, which is a significant improvement over the QSFDTD method. The efficiency of the PCFFT algorithm is such that the 7.2-mm surface charge can be computed in reasonable time on a PC.

5 Conclusions

It is apparent that the hybrid PCFFT+SPFD method is both efficient and accurate, and is the most suitable candidate for modeling low-frequency electric induction in complicated inhomogeneous conductors. The differences obtained among the various modeling approaches used in the present results are clearly far smaller than uncertainties associated with the voxel-based body models themselves.

The most serious defect of voxel-based models is the sharp edges and associated singularities [9], particularly at the (staircased) air-conductor outer boundary. The PCFFT has the added advantage that its implementation is independent of facet geometry. This opens the possibility of future implementation involving solution of the external problem on a smoothed (for example, triangular facets) model of the body surface to alleviate the errors associated with staircasing. Finite element methods could also be used to alleviate staircasing errors, if suitable models were available.

The examples presented here are all based on electrically isolated body models. A more realistic configuration involves a ground plane, with the body either grounded or insulated from it. This situation can be modeled in a crude manner in the present PCFFT code by introducing an actual image model, thereby doubling the computational domain. Future work will address implementing a ground plane in an efficient manner within the PCFFT algorithm.

Acknowledgment :

The authors thank Kris Caputa for his contribution to the development of the human body model and assistance with the QSFDTD runs.

The financial support of this research under an Industrial Research Chair sponsored by NSERC, Bell Alliance and Telus, BC Hydro and TransAlta Utilities is gratefully acknowledged.

References

[1] J. Van Bladel. *Electromagnetic Fields.* Hemisphere Publishing Corporation, Washington D.C., revised printing edition, 1985.

[2] P. J. Dimbylow. Induced current densities from low-frequency magnetic fields in a 2-mm resolution, anatomically realistic model of the body. *Phys. Med. Biol.*, **43**:221–230, 1998.

[3] Jan De Moerloose, Trevor W. Dawson, and Maria A. Stuchly. Application of finite difference time domain algorithm to quasi-static field analysis. *Radio Science*, **32**(2):329–342, March-April 1997.

[4] M. E. Potter, M. Okoniewski, and M.A. Stuchly. Low frequency finite difference time domain FDTD for modeling of induced fields in humans close to line sources. *Journal of Computational Physics*, **162**:221–230, 2000.

[5] Trevor W. Dawson, Jan De Moerloose, and Maria A. Stuchly. Hybrid finite-difference method for high-resolution modelling of low-frequency electric induction in humans. *J. Comp. Phys.*, **136**(2):640–653, September 15th 1997.

[6] Joel Reuben Phillips. *Rapid Solution of Potential Integral Equations in Complicated 3-Dimensional Geometries.* PhD thesis, MIT, 1997.

[7] Trevor W. Dawson, K. Caputa, and Maria A. Stuchly. Organ dosimetry for human exposure to non-uniform 60-Hz magnetic fields. *IEEE Transactions on Power Delivery*, **14**(4):1234–1239, October 1999.

[8] Trevor W. Dawson, Jan De Moerloose, and Maria A. Stuchly. Comparison of magnetically induced ELF fields in humans computed by FDTD and scalar potential FD codes. *Applied Computational Electromagnetics Society Journal*, **11**(3):63–71, November 1996.

[9] T. W. Dawson, M. Potter, and M. A. Stuchly. Evaluation of modeling accuracy of power frequency field interactions with the human body. *Applied Computational Electromagnetics Society Journal*, **16**(2):162–172, July 2001.